AIP | Journal of Applied Physics

Noninvasive probing of the human body with electromagnetic pulses: Modeling of the signal path

F. Thiel and F. Seifert

Citation: J. Appl. Phys. 105, 044904 (2009); doi: 10.1063/1.3077299
View online: http://dx.doi.org/10.1063/1.3077299
View Table of Contents: http://jap.aip.org/resource/1/JAPIAU/v105/i4
Published by the American Institute of Physics.

Noninvasive probing of the human body with electromagnetic pulses: Modeling of the signal path

F. Thiel[a] and F. Seifert
Physikalisch-Technische Bundesanstalt, Braunschweig and Berlin, Abbestr. 2-12, D-10587 Berlin, Germany

(Received 25 June 2008; accepted 1 January 2009; published online 18 February 2009)

The biomedical applications of ultrawideband (UWB) radar promise a very important means to remotely monitor physiological signatures such as myocardial deformation and respiration. Accurate numerical and analytical techniques to predict the propagation of UWB signals in biological tissue are of great interests to researchers as an aid in developing signal processing algorithms. We propose applying an analytic transmit/receive signal path model considering the antennas, the human body, and the signal processing part of the UWB unit. Furthermore, the frequency dependency of the different biological tissues' dielectric properties and the individual continuous motion of intrathoracic tissue layers are incorporated. © *2009 American Institute of Physics*.
[DOI: 10.1063/1.3077299]

I. INTRODUCTION

Microwaves ($0.3\ \mathrm{GHz} < f < 300\ \mathrm{GHz}$) and microwave sensors are used for a wide range of applications: (i) measurement of distance, (ii) speed, (iii) movement, shape, and (iv) particle size, but the largest group of applications is related to the measurement of material properties.[1] A radar (radio detection and ranging) sensor is based on the detection or measurement of the microwaves reflected from an object after short-range free-space propagation. Using broadband signals offers the advantage to gain more object information rather than utilizing a single frequency, e.g., for the observation of the material characteristics' change over a wider frequency range under a certain physical or chemical influence. Furthermore, exposing an object to ultrawideband (UWB) signals (0.1–10 GHz) grants access to a reflection signal proportional to the impulse response function (IRF) of the object, due to their noiselike spectral behavior,[2] and consequently, to the object's frequency response function (FRF). The IRF contains not only the information of the surface of the object but also of its internal structure, since the objects' radar cross section depends on the reflection coefficient which itself depends on the internal composition of the object.[3] The low frequency components of the signal pronounce the deeper structures of the object, whereas the high frequency components pronounce the structures close to the surface due to their reduced penetration depth. The techniques used for this purpose are impulses, stepped sine waves, or pseudonoise (PN) excitation. However, stepped sine waves and PN target stimulation will not provide the IRF directly. It rather requires an appropriate impulse compression technique (i.e., Fourier transform, correlation, or matched filtering). Since all of these three excitation techniques can be made spectrally equivalent, for illustrative purpose we will focus on impulse excitation in this article.

UWB electromagnetic pulses generated by an UWB radar (up to 10 GHz) are able to probe the human body, because electromagnetic waves can propagate through the body and are reflected at interfaces between materials with different dielectric properties.[2,4] This characteristic of UWB radar suggests an ability to monitor the motion of organs within the human body as well as obtaining images of internal structures with a remote noncontact approach which is unique at present. As a result of the distinctive difference in reflection magnitude between the heart muscle and the blood it pushes into the vascular system, UWB radar is able to detect physiological processes noninvasively, e.g., the motion of the myocardial wall. The specific advantages of UWB sensors making them so attractive for biomedical applications are high temporal and spatial resolutions, deep penetration into objects, low integral power (~ 1 mW), and compatibility with established narrowband techniques. The latter one is an essential point, for each critical care unit is equipped with a multitude of devices necessary to monitor the state of the patient. Since nonionizing radiation is used, and due to the ultralow specific absorption rate applied, UWB techniques permit noninvasive sensing at no risk, in contrast to catheter or x-ray techniques and is especially suitable for medical applications including mobile and continuous noncontact supervision of vital functions.

Our research aims at the synergetic use of UWB sounding combined with magnetic resonance imaging (MRI), to gain complementary information, e.g., to accelerate and improve cardiac MR imaging. Respiratory and cardiac displacements introduce motion artifacts in the MR image. With a MR-compatible UWB radar, the characteristic landmarks of the heart's muscle during breathing could be followed without disturbing the actual MR measurement. By means of the position data of the heart which were determined online, it would be possible to subsequently readjust the MR frequency according to the current position of the heart in real time, and also a subsequent position correction of the MR data could be carried out. We have already established a combined MRI/UWB system demonstrating the absence of any interference between both systems, proving the feasibility of the UWB radar method to monitor respiratory and

[a]Electronic mail: florian.thiel@ptb.de.

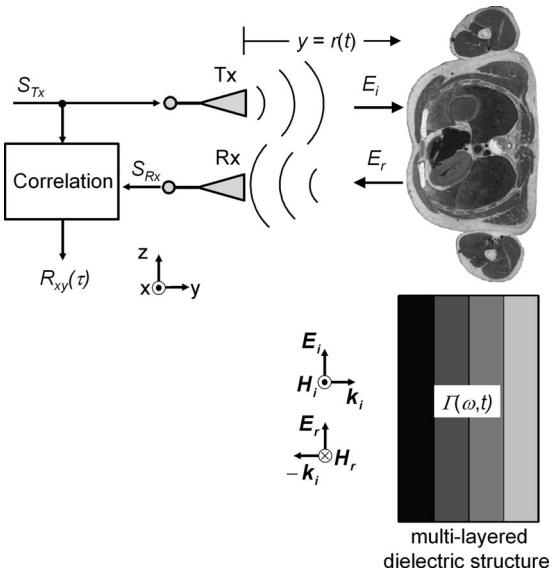

FIG. 1. UWB radar probing a multilayered dielectric structure. S_{Tx}/S_{Rx}: transmitted/received signal. Tx/Rx: transmit/receive antenna. Planar linearly polarized electromagnetic wave: E_i/E_r, H_i/H_r: incident/reflected electrical/magnetical field component. k_i: wave vector of the incident wave. $R_{xy}(\tau)$: correlation result. $\Gamma(\omega)$: reflection coefficient. Anatomic slice taken from (Ref. 6). The transthoracic slice was taken from an appropriate plane through the heart, height of the eighth segment of the thoracic spine (Th8).

myocardial displacements in a 3 T scanner.[5] There are good prospects that the diagnostic quality of the MR imaging of the human heart can be significantly improved with the aid of the MR-UWB technique.

A model representation of the signal path formed by "UWB device/transmitting antenna (Tx)/biological object/receiving antenna (Rx)/UWB device" is crucial for a sound understanding of the measured signals which are formed by the propagation of the electromagnetic waves in layered dielectric media, i.e., the human body, as well as for studying the variation of the reflected signal induced by well-defined layer displacements.

To this end, we propose an analytical model of this transmit/receive signal path, including the signal processing part of the UWB unit, which allows the prediction of the effects of physiological intrathoracic motions on the time courses provided by an UWB radar. These synthetic signals can also be used to test and improve the motion-detection algorithms by introduction of known interfering signals, e.g., antenna ringing, antenna cross-talk, time dependent clutter, or multipath reflections which we exclude from the following analysis.

II. MODELING OF THE EMPTY TRANSMISSION CHANNEL

Figure 1 depicts the setup commonly used to probe the human body with an UWB device. The body can be assumed to form a multilayered dielectric structure with characteristic reflection coefficient $\Gamma(\omega)$. The UWB signal, a pulse, or a PN sequence, creating the same spectral response,[2] of up to 10 GHz bandwidth, is transmitted utilizing appropriate broadband antennas Tx (e.g., the tapered slot or horn antennas). The reflected signal is detected by Rx and the correlation between received signal S_{Rx} and the transmitted signal pulse S_{Tx} is calculated for further signal processing.

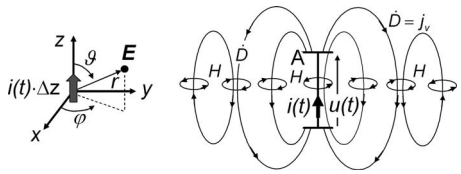

FIG. 2. Left: Hertzian dipole (elementary antenna). Electrical field vector $\boldsymbol{E}=(E_r,E_\vartheta,E_\varphi)$. Right: Simplified antenna. A: area of the capacitor plates; H: magnetic field; $\dot{D}$: displacement current j_v. rot $H=\sigma E+\dot{D}$.

Finite difference time domain (FDTD) techniques are very helpful in simulating the field propagation numerically in static arrangements or in a few selected states. However, if arbitrary time dependencies of $r(t)$ and $\Gamma(\omega,t)$ have to be considered, a (quasi-) continuous analysis is required which can be provided by analytic approaches.

In this chapter we exclude the multilayered object from Fig. 1 and assume an adverse, face to face arrangement of the copolarized antennas. This arrangement forms the empty transmission channel. For signal path modeling, the following assumptions were made: (i) ideal antennas in the sense of mimicking the behavior of an distributed arrangement of simultaneously excited electrical dipoles. (ii) Propagation effects on the antenna, i.e., antenna dispersion, is not considered. (iii) The impedance of the antennas is dominant in comparison to the impedance of the signal source and of the receiver circuit. (iv) Far-field approximation for E_i and for the received reflected electrical field E_r at Rx is assumed. (v) Polarization effects are not considered, i.e., the antennas are copolarized and the normal incidence of the EM wave is assumed. In Secs. III–VIII, this assumption will lead to a propagation normal to each interface of the stratified object; hence no polarization effects occur.

For a simplified transmitting antenna Tx (Fig. 2), the relation between current $i(t)$ and voltage $u(t)$ is as follows:

$$i(t)=\dot{Q}=C\times\dot{u}=\varepsilon_0\varepsilon\times A\dot{E}=A\times\dot{D}, \tag{1}$$

where Q stands for the charge, C stands for the capacitance, A stands for the area of the capacitor plates, D stands for the electric displacement field, and E stands for the electrical near field. Equation (1) also describes the receiving antenna Rx positioned in the far field; hence the received voltage u_{Rx} is proportional to the incident field E_r. The proportionality $i\propto du/dt$ also holds for more complex antennas.[7]

An elementary antenna is appropriately described by a Hertzian dipole (Fig. 2), whose solitary electrical field component in the $\vec{e}_\vartheta$-direction within the far-field approximation becomes

$$E_\vartheta=\frac{j\omega\times i(t)\Delta z}{4\pi}\exp\left(-j\frac{\omega}{c_0}r\right)\left(\frac{\mu}{r}\right)\sin\,\vartheta\cdot\vec{e}_\vartheta, \tag{2}$$

where μ denotes permeability, which can be regarded to be $\mu=\mu_0$ in the channel and in biological tissue, Δz is the length of the current element, and r is the distance from the current element in free space. Therefore, in the time domain the signal in the channel E_ϑ is proportional to $di(t)/dt\times\delta(t-r/c_0)$, where $\delta(t-r/c_0)$ considers the retarded arrival of the

electromagnetic wave at the distance r in free space. When propagating through the antenna, a current pulse is differentiated once and the waveform in the channel is the first derivative of the generated one.[8] By examining the input and output signals of the empty transmission path by means of transfer functions, we have to distinguish between the current transfer function $I_{\mathrm{Rx}}/I_{\mathrm{Tx}}$ and the voltage transfer function $U_{\mathrm{Rx}}/U_{\mathrm{Tx}}$. Hence, from Eqs. (1) and (2) and the assumptions which we have drawn above, for a current driven antenna together with a current analyzing receiver, the relation between the driving current I_{Tx} and the received current I_{Rx} is as follows:

$$I_{\mathrm{Rx}}(t) \propto \dot{U}_{\mathrm{Rx}}(t) \propto \dot{E}_{\vartheta} \propto \ddot{I}_{\mathrm{Tx}}(t). \tag{3}$$

Thus, with Eq. (1) for a voltage driven antenna in conjunction with a voltage analyzing receiver, the relation between the input voltage U_{Tx} and the received voltage U_{Rx} becomes

$$U_{\mathrm{Rx}}(t) \propto E_{\vartheta} \propto \dot{I}_{\mathrm{Tx}}(t) \propto \ddot{U}_{\mathrm{Tx}}(t). \tag{4}$$

In both cases the received signal is proportional to the second derivative of the corresponding transmitted signal. Thus, the receiving and transmitting antenna can be thought of as a differentiator for a current input signal,[9] which means the signal in the channel is the first derivative of the input current signal and the second derivative is carried out by Rx. In contrast, for an input voltage signal the second time derivative for the signal in the channel applies,[10,11] which can be exclusively dedicated to the transmitting antenna Tx.

For a half-wave antenna it was shown in Ref. 12 that the aperture L must not be much greater than the propagation speed c in the antenna material times the duration τ of the wideband pulse applied, in order to keep the validity of Eq. (2). In the case of an antenna array, which can be thought of as a distribution of elementary antennas (Hertzian dipoles) which are excited equally, Eqs. (3) and (4) are always valid. For broadband antennas (horn type, etc.), the energy must pass through a physically distinct aperture, which can be thought of as a continuous distribution of elementary antennas.[7] The resulting **E**-field becomes

$$\mathbf{E} = A_h A_v \mathbf{f}(\vartheta, \phi) \frac{\exp(-j\omega \times r/c_0)}{r}, \tag{5}$$

where A_h and A_v are the beam-forming factors (array factor) for the horizontal and vertical directions, respectively. The function $\mathbf{f}(\vartheta, \varphi)\exp(\cdots)/r$ is the electrical field of each array element which again is proportional to $j\omega \times i(t)$. It is possible to show that the field in the aperture behaves like an equivalent source. This fact is related to Huygens' principle, which states that each element of a wave front may be considered as a secondary source.

III. MODELING OF MOVING MULTILAYERED DIELECTRIC STRUCTURES

To model the influence of the human body in the channel, we implemented a layered tissuelike model. We constructed our model from 14 planar isotropic layers, whose arrangement as well as individual thicknesses approximate a transthoracic slice from the visual human data set[6] (Fig. 3).

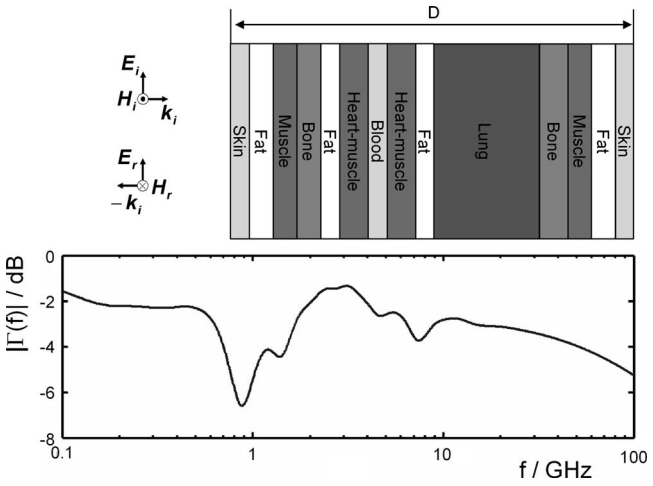

FIG. 3. Top: Layered arrangement to mimic the reflective properties of the human thorax (not to scale). Planar linearly polarized electromagnetic wave: E_i/E_r, H_i/H_r: incident/reflected electrical/magnetical field component. k_i: wave vector of the incident wave. Bottom: Calculated magnitude of the reflection response $\Gamma(f)$ utilizing Eqs. (6) and (7) which is equivalent to the FRF of the object. D: depth of the model in the inflated state=0.2578 m. The thicknesses of each layer in the inflated state from left to right: l_{skin} =3.4 mm, l_{fat}=9.5 mm, l_{muscle}=15.6 mm, l_{bone}=9.5 mm, l_{fat}=9.5 mm, $l_{\mathrm{heart\text{-}muscle}}$=26.6 mm, l_{blood}=22 mm, $l_{\mathrm{heart\text{-}muscle}}$=26.6 mm, l_{fat}=6.2 mm, l_{lung}=91.1 mm, l_{bone}=9.5 mm, l_{muscle}=15.6 mm, l_{fat}=9.5 mm, and l_{skin} =3.4 mm. Exemplary permittivity values: $\varepsilon'(3\ \mathrm{GHz})$: $\varepsilon'_{\mathrm{skin}}$=37.5, $\varepsilon'_{\mathrm{fat}}$ =10.65, $\varepsilon'_{\mathrm{muscle}}$=52.2, $\varepsilon'_{\mathrm{bone}}$=37.5, $\varepsilon'_{\mathrm{heart\text{-}muscle}}$=53.2, $\varepsilon'_{\mathrm{blood}}$=57.3, and $\varepsilon'_{\mathrm{lung\text{-}inflated}}$=20.14.

The transthoracic slice was taken from an appropriate plane through the heart (height of the eighth segment of the thoracic spine, Th8) and we identified the major 14 different layers and their thicknesses in this slice. Each individual slice material is related to a frequency dependent dielectric behavior (Ref. 13 and Fig. 4).

The spectral response of a dielectric medium is appropriately described in terms of multiple Cole–Cole dispersion [Eq. (6)] which, with a choice of parameters appropriate to each constituent, can be used to predict the dielectric behavior over the desired frequency range:[13]

$$\varepsilon(\omega) = \varepsilon_{\infty} + \sum_{m=1}^{4} \frac{\Delta\varepsilon_m}{1 + (j\omega\tau_m)^{(1-\alpha_m)}} + \frac{\sigma_i}{j\omega\varepsilon_0}, \tag{6}$$

where up to 4 Cole–Cole dispersions in the frequency range f=10 Hz–100 GHz are considered. $\omega=2\pi f$; ε_{∞} is the permittivity for $\omega \to \infty$; ε_0 is the permittivity of free space; $\Delta\varepsilon_m$

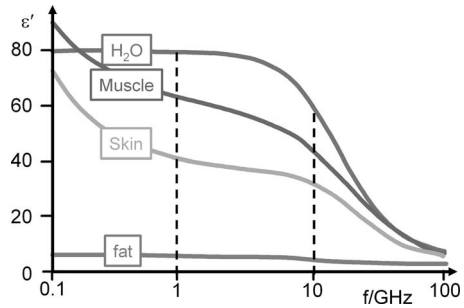

FIG. 4. Frequency dependency of permittivity ε' of high and low water content biological tissues. The dispersion of water dominates the spectral behavior in the UWB frequency range. Adapted from Ref. 13.

is the change of ε in the individual dispersion region; τ_m is the mean time constant of the individual dispersion region; α_m is the distribution parameter describing the broadening of the dispersion, i.e., the broadening of the distribution of time constants around τ_m; and σ_i is the ionic conductivity in the static case. In case of a stationary ε, $\Delta\varepsilon_m=0$ outside the dispersion region, the imaginary part of $\varepsilon=\varepsilon'-j\varepsilon''$ is exclusively determined by the conductivity $\sigma=\varepsilon''\cdot\varepsilon_0\cdot\omega$. The thickness of each slice in the static inflated state and an exemplary value of the real part of permittivity at $\omega=2\pi\times3$ GHz is given in the caption of Fig. 3.

For such a layered arrangement (Fig. 3), the reflection response can be recursively calculated using[14]

$$\Gamma_i(\omega)=\frac{\rho_i+\Gamma_{i+1}e^{-2jk_il_i}}{1+\rho_i\Gamma_{i+1}e^{-2jk_il_i}}, \tag{7}$$

with $i=M,M-1,\ldots,1$, where M is the number of layers. ρ_i is the specific reflection coefficient of each interface, considering the interface of spatially infinite extended dielectric half spaces: $\rho_i=(1-\sqrt{\varepsilon_i/\varepsilon_{i-1}})/(1+\sqrt{\varepsilon_i/\varepsilon_{i-1}})$; Γ_i is the reflection response at the ith interface, initialized by $\Gamma_{M+1}=\rho_{M+1}$. With l_i and $k_i(\varepsilon',\ \varepsilon'')$ we denote the thickness and the propagation parameter, respectively, of the ith layer. ε' denotes the real part and ε'' denotes the imaginary part of complex permittivity ε from Eq. (6).

If the stratified object is located at distance r from the Tx/Rx antennas, now assumed in the resumed adjacent arrangement as depicted in Fig. 1, the ratio of the E-fields in the frequency domain at Rx and Tx becomes (TEM wave)

$$\frac{E_{\mathrm{Rx}}}{E_{\mathrm{Tx}}}(\omega)=\Gamma(\omega)\left[d(r)\exp\left(-2j\frac{\omega}{c_0}r\right)\right]\sim\frac{1}{(j\omega)^2}\frac{S_{\mathrm{Rx}}}{S_{\mathrm{Tx}}}(\omega). \tag{8}$$

To account for the path dependent damping of the electromagnetic wave in the far field, $d(r)$ is introduced. Assuming a spherical wave reflected at a plane, extended surface, the path dependent damping becomes $d(r)=(2r)^{-1}$. The reflection on a point target would again be the source of a spherical wave which results in $d(r)=r^{-2}$.

Since respiratory motion changes r by around 10 mm[15] and cardiac contraction also moves the surface of the thorax by an amplitude of ~1 mm,[16] time dependences $r(t)$ and $\Gamma(\omega,t)$ are introduced (Figs. 1 and 3). An additional time dependency is introduced in the reflection coefficient by the displacement of intrathoracic layers which must not necessarily be transmitted to the body's surface.

Given that, the received signal S_{Rx} in the frequency domain becomes

$$S_{\mathrm{Rx}}=[S_{\mathrm{Tx}}H_{\mathrm{Tx}}H_{\mathrm{Rx}}\Gamma\ \exp(-2j\omega r/c_0)d(r)], \tag{9}$$

with H_{Tx} and H_{Rx} representing the transfer functions of the transmitting and receiving antennas, respectively.

The exponential function accounts for the time delay between the transmitted and received signals due to the propagation in free space. With S_{Tx} being an even function [$f(-x)=f(x)$], finally, the output of the correlator in Fig. 1 becomes

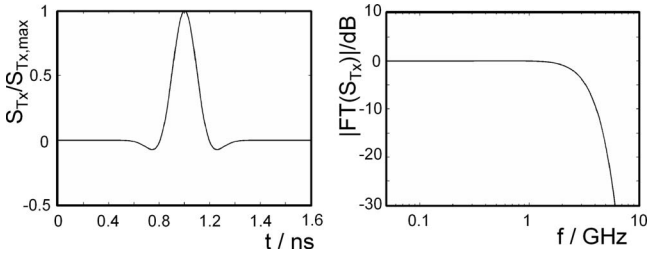

FIG. 5. Left: Normalized transmitted S_{Tx} pulse ($f_C=3$ GHz, pulse width $\tau_p\sim0.15$ ns). Right: Amplitude spectrum $|\mathrm{FT}(S_{\mathrm{Tx}})|$ of the transmitted pulse. FT stands for the Fourier transform.

$$R_{xy}(\tau)=\int S_{\mathrm{Tx}}(t+\tau)S_{\mathrm{Rx}}(t)dt$$
$$=S_{\mathrm{Tx}}(-\tau)\circ S_{\mathrm{Rx}}(\tau)=S_{\mathrm{Tx}}(\tau)\circ S_{\mathrm{Rx}}(\tau). \tag{10}$$

There "$\circ$" represents the convolution operator.

IV. ULTRAWIDEBAND PULSES

We utilized an M-sequence UWB radar system (up to 5 GHz) transmitting a periodic pseudorandom waveform (maximum length binary sequence) to measure the IRF of the object under test.[2] The spectral representation of such PN sequences can also be equivalently formed by an appropriate impulse. Together with the aspect that the following analysis becomes not very illustrative in the time domain using M-sequences, we will use an equivalent pulse below.

A typical class of such broadband pulses are those of the Gaussian shape and their derivatives.[11] The waveform used in further studies is a modified Ricker pulse, which is formed from the second derivate of the Gaussian pulse. The general zero-mean Gaussian pulse $p_G(t)$ is derived by

$$p_G(t)\sim\exp\left(-2\pi\frac{t^2}{\tau_0^2}\right), \tag{11}$$

where τ_0 is the pulse duration. Therefore, the Ricker pulse can be described by

$$p_R(t)=(2\beta-1)\exp(-\beta), \tag{12}$$

where

$$\beta=2\pi t^2/\tau_0^2. \tag{13}$$

A broadband pulse, whose spectral behavior is similar to the excitation signal we apply (flat spectrum down to several megahertz, -3dB at 3 GHz) in our envisaged medical application,[5] can be formed from p_R (Fig. 5)

$$S_{\mathrm{Tx}}(t)=\left(\frac{1}{3}\beta-1\right)\exp\left(-\frac{\beta}{2.5}\right). \tag{14}$$

The band-limiting effect is then introduced by the antennas applied.

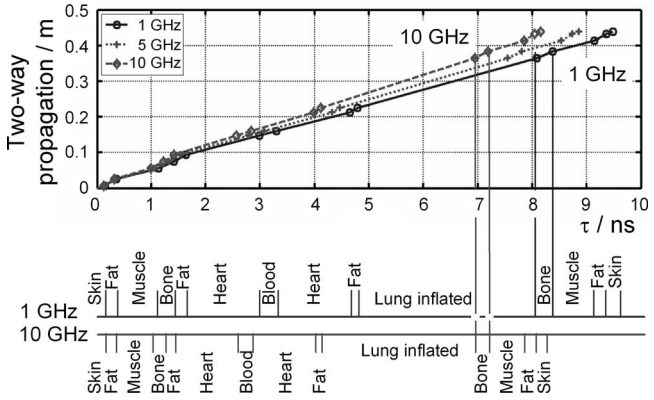

FIG. 6. Calculated propagation vs propagation time (τ) for three different frequencies. Propagation times to reach a certain interface are indicated below the τ-axis for 1 and 10 GHz signals.

V. RESULTS

A. Propagation time and power losses

From the layered model we can calculate the evolution of the propagation time and power losses while the electromagnetic waves traverse each layer at different frequencies (Figs. 6 and 7).

The two-way propagation time to propagate through and back the ith layer of thickness $\Delta y = l_i$ in the forward y-direction is defined by

$$\tau_i = 2\frac{l_i}{c_0}\sqrt{\varepsilon_i'}. \tag{15}$$

For biological tissue, the real part of the permittivity $\varepsilon(\omega)$ decreases with increasing frequency;[13] e.g., $\varepsilon'(1\ \text{GHz})/\varepsilon'(10\ \text{GHz}) = 1.5$ for muscle tissue. This results in a shortened propagation time $\tau_i(10\ \text{GHz}) = 1/\sqrt{1.5}\tau_i(1\ \text{GHz})$. Figure 6 depicts the calculated two-way propagation versus the one-way propagation time τ for three different frequencies.

The power per unit area flowing past the point y in the forward y-direction will be

$$P(y) = P(0)e^{-2\alpha y}, \tag{16}$$

where α denotes the attenuation constant:

$$\alpha = \text{Re}\{\omega\sqrt{\mu[\varepsilon'(\omega) - j\varepsilon''(\omega)]}\}. \tag{17}$$

Hence, the power loss in decibels in a layer of thickness Δy becomes

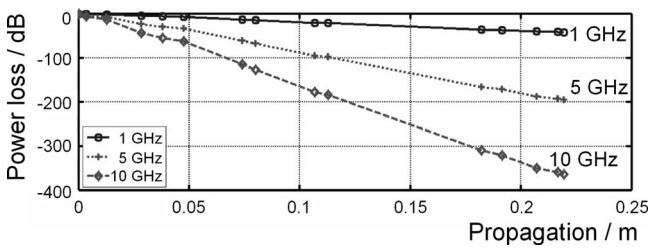

FIG. 7. Power losses vs penetration depth of an electromagnetic wave while traversing the 14-layer model computed for different frequencies as indicated by the legend.

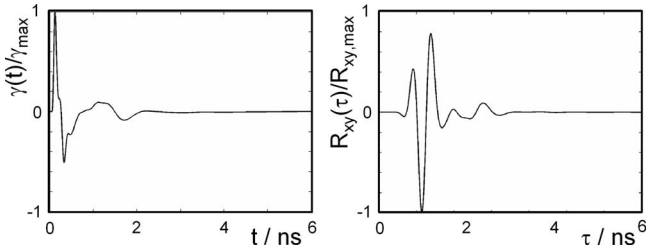

FIG. 8. Left: Normalized IRF $[\gamma(t)]$ of the multilayered dielectric structure. Right: Normalized result of the correlation $R_{xy}(\tau)$ between the signals S_{Rx} and S_{Tx}.

$$A_{\text{dB}} = -10\log_{10}\left[\frac{P(\Delta y)}{P(0)}\right] \approx 8.686\Delta y\alpha. \tag{18}$$

Figure 7 depicts the evolution of the power losses versus penetration depth of an electromagnetic wave (1, 5, and 10 GHz) while traversing the layered model.

This sketch implies helpful information for application-dependent antenna design.[17] With the aim of monitoring myocardial function at its origin, the electromagnetic wave should reach the heart muscle which can be expected at a depth of around 40 mm (sixth layer, path through the breast muscle and fat) in the worst case. The best case is given by a propagation way right through the sternum. Application of a 1 GHz signal implies penetration through the whole body, with a signal attenuation of about 50 dB at the back. With an appropriate receiver, and signal processing techniques, myocardial deformation should be detectable even with frequencies up to 10 GHz. A further hint for the detectability of myocardial deformation at its origin by UWB radar is given by the comparison of the reflection coefficient of the 14-layer model with the result obtained from a layer stripped model. We found out that at least the first 6 layers are required to closely approximate the response given by the whole 14-layer model for frequencies above 1 GHz. Since the sixth layer represents the frontal myocardial muscle, its variations should be visible in the reflection signal.

B. Impulse response and correlation result

From $\Gamma(\omega)$, the IRF follows in the time domain by applying inverse Fourier transform F^{-1} (Fig. 8, left):

$$\gamma(t) = F^{-1}\{\Gamma(\omega)\}. \tag{19}$$

In this way the output of the correlator can be calculated applying Eqs. (8) and (10), and is depicted on the right of (Fig. 8).

Since the reflected signal is represented by convolving the IRF with the incident signal, in our special case the reflected signal can be thought of as being the result of the convolution of the IRF with the Dirac distribution represented by our broadband pulse. This being the case, the reflected signal is similar in shape to the IRF of the material under test.

The complete signal path model for both cases, voltage transfer function and current transfer function, is depicted in

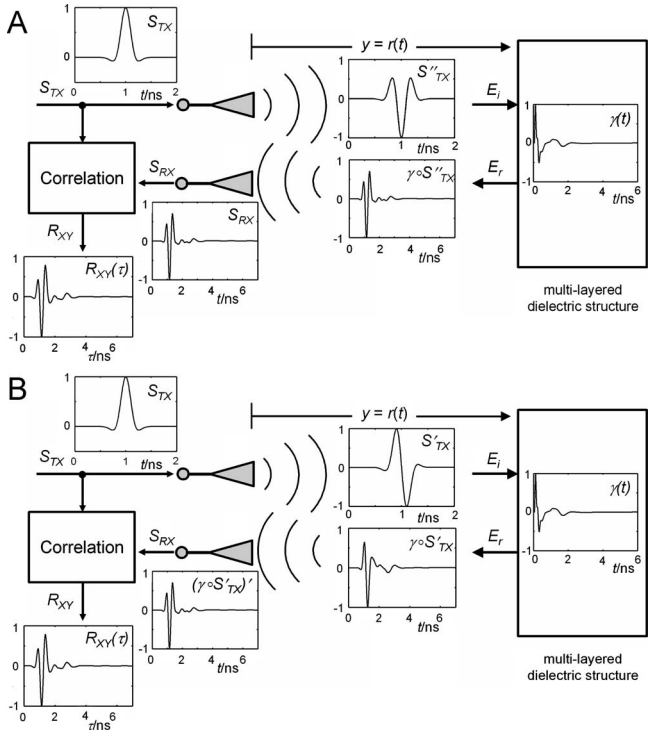

FIG. 9. Sketch of the complete signal path model: (A) the voltage transfer function $S_{Rx}/S_{Tx}=U_{Rx}/U_{Tx}$ and (B) for the current transfer function $S_{Rx}/S_{Tx}=I_{Rx}/I_{Tx}$. Upper (A): S_{Tx}: excitation voltage signal/pulse. $S''_{Tx}=E_i$: free-space signal in the channel. E_i: incident electrical field component. γ: IRF of the multilayered dielectric structure in the time domain. $S''_{Tx}\circ\gamma=E_r$: reflected electrical field component. $S_{Rx}=E_r(r)$: received voltage signal/pulse. Lower (B): S_{Tx}: excitation current signal/pulse. $S'_{Tx}=E_i$: signal in the channel. $\gamma\circ S'_{Tx}=E_r$: reflected electrical field component. $(\gamma\circ S'_{Tx})'$: received current signal/pulse. $R_{xy}(\tau)$: output signal of the cross-correlation process between S_{Tx} and S_{Rx} [in units of V^2 s (case A) or A^2 s (case B), respectively].

Fig. 9 comprising the signals in the time domain for each relevant intermediate step between excitation signal S_{Tx} and output signal R_{xy} (τ).

VI. MODELING OF PHYSIOLOGICAL EVENTS

To get a feeling of how myocardial deformation influences the reflection coefficient, both in the frequency and the time domain, we modeled the end-systolic and end-diastolic states of the heart by the variation in the layer representing the blood volume in the heart by 10 mm. The two heart muscle layers vary antipodally by 5 mm, accordingly. The results are depicted in Fig. 10. The largest variations arise between 1 and 2 GHz with a maximum at 1.1 GHz with 0.013 dB. The largest variation in the IRFs occurs with 2.3×10^{-6} (~-112 dB) at $\tau_{SD}=5$ ns, where the heart-related layers are located in the model. According to the results given in Fig. 6, myocardial variations are expected in the time range 3 ns$<\tau<$9 ns (two-way propagation) which agrees very well with τ_{SD}. The propagation way through the sternum, where the heart layer lies close beneath the surface, will of course give much larger signals. Hence, our calculations give a lower bound estimation of expected signals.

To compare the simulation results with real measurements, tissue phantoms are needed mimicking dielectric properties of biological tissue in the frequency range covered

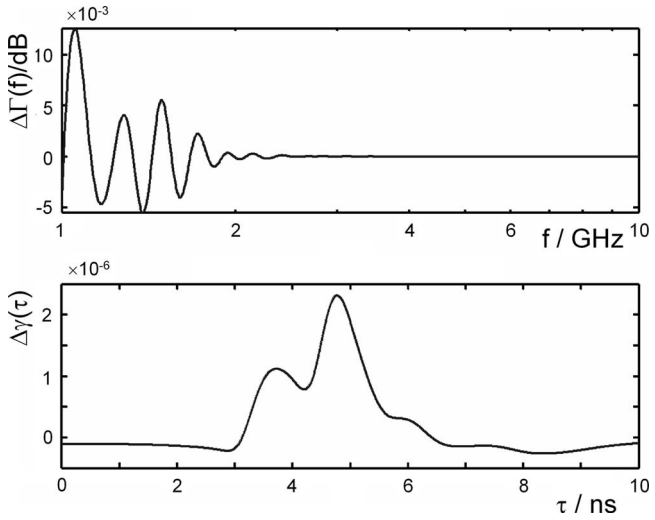

FIG. 10. Comparison of the reflection coefficient in the frequency domain $[\Delta\Gamma=\Gamma_{syst}(f)/\mathrm{dB}-\Gamma_{dias}(f)/\mathrm{dB}]$ and in the time domain $[\Delta\gamma=[\gamma_{syst}(\tau)-\gamma_{dias}(\tau)]/\gamma_{dias}(\tau)$, $\gamma_{syst}(\tau)=$systolic phase, and $\gamma_{dias}(\tau)=$diastolic phase] for the systolic and diastolic phases of the heart modeled by variation in the layer representing the blood volume in the heart by 10 mm. The two heart muscle layers vary antipodally by 5 mm.

by UWB technology (1–10 GHz). We have developed such multilayer phantoms.[18] When exposed to electromagnetic waves in the frequency range of 1–10 GHz, these phantoms provide reflection signals similar to those of the human thorax. These dielectric phantoms were built from planar disk-shaped slices (arbitrary thickness l_i, ∅150 mm) utilizing an oil-in-water emulsion stabilized in an agarose gel. Materials with low permittivity ε', like fat (adipose) tissue, are formed by a silicon gel. To account for the limited conductivity of adipose tissue the silicon gel (Sylgard A&B) is doped with glycerol (propane-1,2,3-triol). The dielectric phantoms were arranged in a sandwich structure, to mimic the sequence of biological tissue layers of the human thorax. The reflection signals of the human thorax can be sufficiently achieved using a phantom consisting of the first three layers of the thorax (skin, fat, and muscle).

A comparison of a measured and the simulated result $R_{xy}(\tau)$ of such a three layered human body phantom[18] is presented in Fig. 11 (upper graph). For the detailed measurement setup, see Ref. 5. Background scatter signals were subtracted from the measured $R_{xy}(\tau)$ in Fig. 11 but the experimental data still include the antenna effects causing minor deviations from the simulations.

We further modeled the continuous physiological process of breathing by a sinusoidal motion with a peak-to-peak amplitude of 10 mm and frequency of 0.2 Hz,[15] superimposed by a continuous, cardiac-induced motion of the thorax surface with a peak-to-peak amplitude of 1 mm[16] and a frequency of 1 Hz. The thickness of the lung layer varies simultaneously with the breathing process. The thickness of the intracardiac blood layer is modulated by the antipodal motion of the two heart muscle layers by 10 mm.

The result is shown in Fig. 11 on the lower graph. In Sec. VII, we used these artificial signals to test an algorithm to extract the motion of the surface from these data.

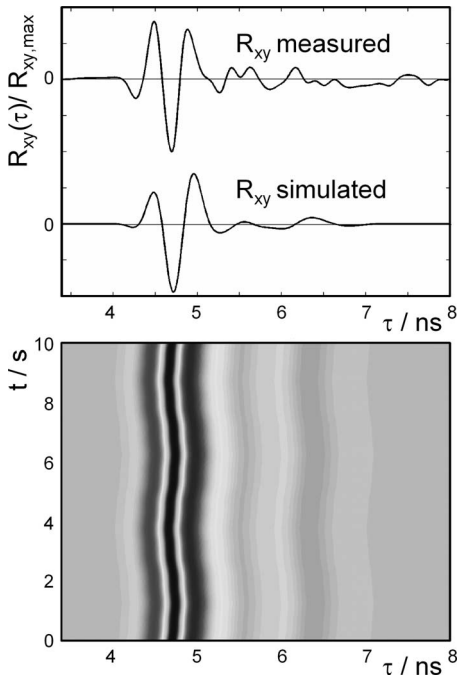

FIG. 11. Upper: Comparison of normalized measured and simulated correlation result $R_{xy}(\tau)$ from the human body phantom. Lower: Simulated time evolution of $R_{xy}(\tau,t)$ during two breathing cycles. Breathing with 10 mm amplitude and 0.2 Hz superimposed by a cardiac-induced motion of the thorax surface of 1 mm with 1 Hz. The lung layer varies by 10 mm. The thickness of the intracardiac blood layer is modulated by the antipodal motion of the two heart muscle layers by 10 mm.

VII. TEST OF MOTION-DETECTION ALGORITHM

To extract displacements of interfaces built from various biological tissues or multilayered phantoms, a number of algorithms were developed and tested. These algorithms are crucial to identify relevant signals in static and dynamic clutters, as well as to decompose significant physiological signatures from the multiple superimposed impulse responses generated by the object under test. Our algorithms are based on an analysis of eigenvalues, extracted from the covariance matrix $\mathbf{Q}$ calculated from the cross-correlation data $R_{xy}(\tau)$ of the transmitted and received signals. $R_{xy}(\tau)$ is provided by the UWB controller where each of the N rows is an observation containing M samples, and each of the M columns represents a time shift $\Delta\tau$. If we define the rows of R_{xy} to correspond to all measurements of a particular type and each column to a set of measurements from one particular trial, the covariance matrix becomes $\mathbf{Q}=1/(N-1)R_{xy}R_{xy}^T$. $\mathbf{Q}$ captures the correlation between all pairs of measurements. The covariance measures the degree of the linear relationship between two variables, where a large (small) value indicates high (low) redundancy. The main diagonal elements $\boldsymbol{\lambda}_Q=\{\lambda_{Q,11},\ldots,\lambda_{Q,MM}\}$ of $\mathbf{Q}$ are the variance of particular measurement types and the off-diagonal terms are the covariance between measurement types. In the diagonal terms, the interesting dynamic is reflected. Given that, we ignore redundancy information by setting the off-diagonal terms to zero, which results in a diagonal matrix $\mathbf{D}$:

$$\mathbf{D}=\mathrm{diag}(\boldsymbol{\lambda}_Q). \tag{20}$$

Therefore $\boldsymbol{\lambda}_Q$ contains the eigenvalues of the diagonal matrix $\mathbf{D}$ for each time shift τ which is an estimate of the momentary signal variance. Each eigenvalue corresponds to a certain time shift τ:

$$M(\tau)=\boldsymbol{\lambda}_Q(\tau). \tag{21}$$

$M(\tau)$ displays the signal variance at each propagation time. Thus, significant values in $M(\tau)$ correspond to relevant interfaces (large Γ), which are displaced by physiological events (Fig. 3). This means that interfaces exhibiting high dielectric contrast, e.g., a fat/muscle interface, produce large reflections, i.e., a large peak with a steep slope in the IRF at the propagation time which corresponds to this interface (see Figs. 6 and 10). Hence, displacements of this IRF creates a large signal at the position of the slope and our algorithm searches for these propagation times, because the $M(\tau)$ displays the signal variance at each propagation time. The interfaces which we state as "relevant" are such high contrast interfaces the air/skin interface and the fat/pericardium/myocardium interface.

We applied this algorithm to the simulated signals from Fig. 11 (lower) and found good agreement between the reference time course and the reconstructed motion from the surface (Fig. 12).

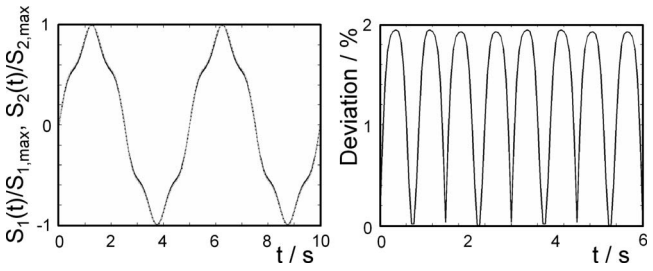

FIG. 12. Left: Comparison of the normalized reconstructed motion ($S_1/S_{1,\max}$, light gray dashed line) from a surface signal with the normalized reference signal ($S_2/S_{2,\max}$, dark bold line). Right: Deviation $||S_1|-|S_2||/S_{2,\max}$.

The absolute deviation from the reference related to the maximal amplitude of the reference is smaller than 2% and is caused by the nonlinearity of the transfer function introduced by the algorithm. Since our transfer function is formed from the flange of a certain interface reflection in the IRF, its linearity is only guaranteed for small displacements like those we expect by respiratory and myocardial events. The deeper the interesting interface lies in the depth of the body, the flatter becomes the transfer function due to the dispersive effects, i.e., the sensitivity decreases. The above calculated deviation is equivalent to a reconstruction uncertainty of 100 μm (2% of 5 mm).

VIII. DISCUSSION

The UWB electromagnetic signals generated by an UWB radar and transmitted by an antenna are able to probe the human body with low integral power, because electromagnetic waves can propagate through the body and are reflected at interfaces between materials with different dielectric properties. The receiving antenna detects the reflected signals coming from different depths of the body.

Motion, induced by respiration or cardiac deformation, displaces and deforms these interfaces and influences the re-

flected signal. For the reconstruction of spatially dependent displacements, special algorithms are needed.

In this regard a model representation of the whole system is crucial for a sound understanding of the propagation of electromagnetic waves in stratified dielectric media as well as for studying the variation of the reflected signal induced by well-defined layer displacements.

We developed and implemented an analytic signal path model considering the antennas, the human body, and the signal processing part of the UWB unit. Especially the broadband frequency dependence of the complex dielectric properties of individual biological tissues was incorporated.

The individual continuous motion of intrathoracic layers was also included in the simulation of physiological signatures. In this way, the influence of physiological processes such as breathing and cardiac motion on the reflection coefficient, and therefore the reflected signal and $R_{xy}(\tau)$ can be modeled and studied independently or in superposition.

With these artificial signals different motion reconstruction algorithms can now be tested and improved. Furthermore, the robustness of the algorithms to perturbations which can be deliberately built into the model, such as antenna ringing, antenna cross-talk, time dependent clutter, or multipath reflections, can be evaluated.

Additionally, this model is helpful for biomedical applications of UWB radar, since it gives a feeling of how propagation time and power losses evolve while the electromagnetic waves traverse each layer. It is therefore beneficial for application-dependent antenna design. Since the number of dielectric layers needed for an UWB radar phantom can be determined to achieve a reflection coefficient closely approximating the reflective properties of the human thorax, this model is also helpful for the design of UWB phantoms.

To account for the perturbation effects introduced by real antennas (dispersion, additional reflection, etc.), the calculated signals from FDTD simulations of the antennas can be implemented.

ACKNOWLEDGMENTS

The authors are grateful to M. A. Hein, R. Stephan and U. Schwarz from Technische Universität Ilmenau for providing the antennas and to J. Sachs and M. Helbig from Technische Universität Ilmenau for their support. This work was supported by the German Research Foundation (DFG) in the priority program UKoLoS (Contract No. SPP1202, project acronym *ultraMEDIS*).

[1] E. Nyfors, *Subsurface Sensing Technologies and Applications* (Springer, Germany, 2000), Vol. 1, pp. 23–43.
[2] J. Sachs, S. Wöckel, R. Herrmann, M. Kmec, R. Zetik, and P. Peyerl, Meas. Sci. Technol. **18**, 1074 (2007).
[3] B. R. Mahafza and A. Z. Elsherbeni, *Simulations for Radar System Design* (Chapman and Hall, London/CRC, Boca Raton, FL, 2004), p. 501.
[4] M. A. Stuchly, *Applications of Microwaves in Medicine*, IEEE AP-S Lecture, 2006 (unpublished).
[5] F. Thiel, M. Hein, J. Sachs, U. Schwarz, and F. Seifert, Rev. Sci. Instrum. **80**, 014302 (2009).
[6] The Visible Human Project, NLM, Bethesda, MD, http://www.nlm.nih.gov.
[7] K. I. Thomassen, *Introduction to Microwave Fields and Circuits* (Prentice-Hall, Englewood Cliffs, NJ, 1971).
[8] K. Siwiak and D. McKeown, *Ultra-Wideband Radio Technology* (Wiley, Chichester, 2004).
[9] J. Taylor, *Introduction to Ultra-Wideband Radar Systems* (CRC, Boca Raton, FL,1994).
[10] G. Barrie, UWB Impulse Radar Characterization and Processing Techniques, Defence R&D Canada-Ottawa, National Defence Headquarters, Ottawa, CA, 2004, p. 22.
[11] M. Hämäläinen, "Singleband UWB systems," PhD. thesis, University of Oulu, 2006.
[12] I. J. Immoreev and A. N. Sinyavin, Radio physics and radio astronomy **7**, 389 (2002).
[13] S. Gabriel, R. W. Lau, and C. Gabriel, Phys. Med. Biol. **41**, 2251 (1996).
[14] S. J. Orphanidis, *Electromagnetic Waves and Antennas* (Rutgers University, New Brunswick, 2008), p. 118.
[15] T. Kondo, T. Uhlig, P. Pemberton, and P. D. Sly, Eur. Respir. J. **10**, 1865 (1997).
[16] G. Ramachandran and M. Singh, Med. Biol. Eng. Comput. **27**, 525 (1989).
[17] U. Schwarz, M. Helbig, J. Sachs, F. Seifert, R. Stephan, F. Thiel, and M. Hein, *Physically small and tuneable double ridged horn antenna for biomedical UWB radar applications* (IEEE ICUWB, 2008), Vol. 1, pp. 5–8.
[18] F. Thiel, F. Schubert, W. Hoffmann, and F. Seifert, Proc. Intl. Soc. Mag. Reson. Med. **16**, 1054 (2008).